Journal of Computational and Applied Mechanics, Vol. 17, No. 1, (2022), pp. 15–43
DOI: 10.32973/jcam.2022.002

MODELING RAPID SOLIDIFICATION AND MELTING PROCESSES FOR MULTIPHASE FLOWS IN A WELDING TECHNOLOGY APPLICATION

Xin Xiong
Centre for Computational Engineering Sciences, Cranfield University,
Cranfield, Bedfordshire, MK43 0AL, United Kingdom
xin.xiong@cranfield.ac.uk

László Könözsy
Centre for Computational Engineering Sciences, Cranfield University,
Cranfield, Bedfordshire, MK43 0AL, United Kingdom
laszlo.konozsy@cranfield.ac.uk

[Received: March 20, 2022; Accepted: May 9, 2022]

Abstract. This article presents unsteady simulations of laser welding based on a rapid solidification/melting model using the ANSYS-FLUENT software package with the implementation of a UDF (User Defined Function) C code. It assumes a flat interface of liquid and gas without plasma plume, evaporation and reflection and absorption effect. In the simulations, a variety of parameters are considered with different welding speeds and laser powers. The results show that with the increase of laser power, liquid fraction and velocity, penetration depth and bead width all increase. In contrary, with the increase of welding speed, the temperature, liquid fraction, penetration depth, and bead width all decrease, while the velocity magnitude is an exception. It has also been found that the increase of welding speed distorts the pool shape and forms a long tail in temperature, liquid fraction and velocity contour. The buoyancy force did not have a significant impact on the results, while the convective term makes the velocity, temperature and liquid fraction smaller. Furthermore, the negative Marangoni shear stress makes the velocity along the height and the width direction smaller in the middle of the workpiece and larger on the edges. The simulation results show a similar tendency to that obtained by other authors. The reason for the possible differences is due to the unsteadiness of the fluid flow field and the slightly different boundary conditions imposed in the model presented here. The novelties of this work are unsteady simulations, new boundary conditions and parametric studies relevant to industrial applications.

Mathematical Subject Classification: 76G25, 76M12, 76F60, 76F55
Keywords: Rapid Solidification/Melting, Laser Welding, Laser Power, Welding Speed, Computational Fluid Dynamics (CFD), Engineering

1. Introduction

Laser welding has many advantageous features over traditional welding techniques such as spot resistance welding. Due to the fact that the laser power and speed can be controlled precisely, laser welding can be accurate and flexible. According to Steen [1], laser welding can be utilized in many regimes such as electronics, medical devices, automobiles, dies, and tools. It overcomes certain problems that traditional welding has with its high energy intensity. The process of laser welding can be described as follows: a) a high intensity laser beam is irradiated on the workpiece, and once the laser beam reaches the workpiece and its temperature exceeds the melting point, it begins to melt; b) after melting, a molten pool is formed with the further irradiation of the laser beam, and the liquid in the molten pool starts to evaporate, which will further form the keyhole; c) during the evaporation process, recoil pressure is created, which further drives the liquid flow outward from the molten pool; d) once the keyhole is formed, it will generate a plasma plume, which will scatter and absorb part of the laser energy, thus reducing the absorption of the objective surface.

To accurately examine the dynamics of the keyhole and the molten pool, different experimental methods have been devised such as cameras, photo diodes, spectrometer, acoustic sensor, pyrometer, and plasma charge sensor according to Shin et al. [2]. Eriksson et al. [3] utilized high speed photography to successfully visualize the dynamics of the molten pool and the keyhole. Normann et al. [4] successfully combined theoretical analysis and photo diodes to monitor the defects of laser welding. Zhang et al. [5] also examined the defect of workpieces using a spectrometer. Although different experiment measurement methods exist to investigate the dynamics of keyholes and molten pooleach has several drawbacks. Another option is Computational Fluid Dynamics (CFD), an advanced computational approach that is widely used in both academic research and industrial areas.

In the case of this specific problem, researchers conducted CFD simulations. First of all, researchers developed simplified theoretical models. For example, Swift-Hook and Gick [6] developed a theoretical analysis based on the solution of the heat diffusion equation. Lankalapalli et al. [7] developed a two-dimensional model with the assumption of a conical keyhole. Dowden et al. [8] analyzed the effect of plasma, combining the plasma model with a simple line heat source model. Secondly, researchers studied this problem using the Finite Element Method (FEM) without consideration of the fluid flow field. For example, Carmignani et al. [9] predicted residual stress and strains using FEM. In the work of Mares et al. [9], an elasto-viscoplastic constitutive equation was added to model the plastic material. Another model is the enthalpy-porosity model to consider the phase change of the workpiece between the solid and the liquid phases. Ye and Chen [10] investigated the three-dimensional effect of the surface tension and the density together assumed to be linear functions of the temperature.

Other models based on free surface tracking algorithms are the level-set method and the VOF (Volume-of-Fluid) method. The level-set method is a self-consistent free surface tracking approach, according to Mohanty and Mazumder [11]. It introduces an equation of motion of interface as a scalar conservation law with viscosity and boundary conditions for the laser welding model [11]. Geiger et al. [12] modeled the joining of zinc coated sheets. They used an open-source software package called OpenFOAM with the VOF model. They also implemented the Gaussian distribution as a surface heat source. They considered the Fresnel absorption, evaporation pressure and surface tension in their computational model. Because of the evaporation effect, it was found that there are low frequency oscillations in the melt pool and high frequency oscillations on the keyhole.

In this paper, a novel unsteady CFD simulation approach for the laser welding model is developed and presented. The effects of surface tension, unsteady fluid flow field, non-isothermal effect, natural convection, heat conduction and melting effects have been considered to provide numerical results that are compared with the work of Abderrazak et al. [13]. The implementation of the additional source terms of the rapid solidification and melting model is carried out in the ANSYS-FLUENT software package within the framework of the solidification and melting model using User-Defined Functions (UDFs), which are computer codes written in C programming language. The structure of the present work can be described as follows: Section 2 describes the governing equations; Section 3 focuses on the mesh and the geometrical model, including mesh sensitivity and time-step studies; Section 4 is the discussion of the computational resultsm which includes the parametric studies; and Section 5 addresses conclusions and recommendations for future work.

2. Governing Equations and Methodology

The governing equation of the rapid solidification model presented here is based on the enthalpy-porosity model. This model combines the solid and liquid equations as a single equation, which was also considered by Abderrazak et al. [13]. The continuity equation of three-dimensional fluid flows can be expressed by

$$\frac{\partial \rho}{\partial t} + \frac{\partial (\rho u)}{\partial x} + \frac{\partial (\rho v)}{\partial y} + \frac{\partial (\rho w)}{\partial z} = 0, \tag{2.1}$$

where ρ is the density of the material, t is the time for unsteady simulations, x, y, z are the Cartesian coordinates, u, v, w are the velocity components of the fluid flow in x, y and z directions, respectively. The scalar momentum equations are

$$\frac{\partial \rho u}{\partial t} + \nabla \cdot (\rho u \vec{u}) = -\frac{\partial p}{\partial x} + \nabla \cdot (\mu \nabla u) - \frac{\mu}{K}(u - u_x), \tag{2.2}$$

$$\frac{\partial \rho v}{\partial t} + \nabla \cdot (\rho v \vec{u}) = -\frac{\partial p}{\partial y} + \nabla \cdot (\mu \nabla v) - \frac{\mu}{K} v, \tag{2.3}$$

$$\frac{\partial \rho w}{\partial t} + \nabla \cdot (\rho w \vec{u}) = -\frac{\partial p}{\partial z} + \nabla \cdot (\mu \nabla w) - \frac{\mu}{K} w + \rho g \beta (T - T_{\text{ref}}), \tag{2.4}$$

where p is the pressure, $\vec{u}$ is the velocity vector, K is the permeability coefficient, μ is the dynamic viscosity, u_x is the welding speed in x direction, β is the thermal expansion coefficient, g is the magnitude of the gravitational acceleration, T is the temperature, and T_{ref} is the reference temperature. The energy equation is modeled as

$$\rho C_p \left(\frac{\partial T}{\partial t} + \nabla \cdot (T \vec{u}_1) \right) = \nabla \cdot (k \nabla T) + S(x, y, z) - \nabla \cdot ((\rho \vec{u}) \Delta H), \tag{2.5}$$

where $\vec{u}_1$ is the fluid velocity, which are $u - v_w$, v, w in x, y, z directions, v_w is the welding speed, $\vec{u}$ is the velocity, which are u, v, w in x, y, z directions, C_p is the specific heat, k is the heat conduction coefficient, S is the additional heat source, ΔH is the latent heat. A Gaussian volume heat source was implemented in this model as

$$Q(x,y,z) = \frac{3P}{\pi abd} \exp\left(-\frac{3x^2}{a^2}\right) \exp\left(-\frac{3y^2}{b^2}\right) \exp\left(-\frac{3z^2}{d^2}\right), \tag{2.6}$$

where $Q(x,y,z)$ is the heat source, P is the power of laser beam, a, b, d are the length, width and depth of the laser beam, respectively. The boundary condition of the bottom surface is a convective boundary condition

$$q_{\mathrm{c}} = h_{\mathrm{ext}}\left(T_{\mathrm{ext}} - \mathrm{T_w}\right), \tag{2.7}$$

where q_c is the convective heat energy, h_{ext} is the convective heat transfer coefficient, T_{ext} is the exterior temperature, and T_w is the temperature of the bottom wall where the convective effect was set to be considered. The surface convection is only allowed between the bottom wall and the environment. The boundary condition of top surface is a constant shear stress as described below:

$$\mu\frac{\partial u}{\partial z} = C, \tag{2.8}$$

where C is a constant and the left term represents shear stress. This is different from the work of Abderrazak et al. [13], because in their work [13], the shear stress is used to model the negative Marangoni effect, which is related to the temperature gradient. However, the temperature gradient in this model is very small. Thus, the influence of the temperature gradient can be ignored, and thus constant shear stress is assumed here to simplify the model. The other boundary condition is set to a constant temperature of 300 K, except for the bottom wall.

In this model, thermal expansion is allowed in the normal direction, which can be seen from the z-momentum equation with the expansion term. The top wall is modeled as a flat surface model in this work. For the sake of simplicity, the solid top wall has been considered to be a rigid wall.

The material properties of the model are considered to be constant, except for the density, which is predicted based on the Boussinesq assumption. The thermal conductivity k has been considered as constant within the same phase as a modeling simplification. This simplification follows the model description of Abderrazak et al. [13], where the thermal conductivity was considered to be constant for each phase. Large temperature differences can be observed in the middle of the domain. The dynamic viscosity μ is constant for the liquid phase. Furthermore, the permeability parameter K is used to model the phase change, which is derived from the Kozeny–Carman equation [13] to make a smooth transition between two phases. Therefore, a unified equation is solved for both phases. When a solid phase is considered during the process, K is a very small value and the fluid flow velocity is approximately zero in the y and z directions, while K is equal to the welding speed in direction x. When melting occurs during the welding process, the permeability parameter K becomes a very large value.

3. Computational Domain, Mesh Sensitivity and Time-Step Study

As can be seen from Figure 1, the workpiece moved with the welding speed and a laser beam is introduced from above. The physical domain of this engineering problem is considered to be rectangular. The computational mesh is a structured mesh due to the simplicity of the rectangular geometry. Three mesh densities were generated to study the mesh sensitivity for the numerical solution (Table 1).

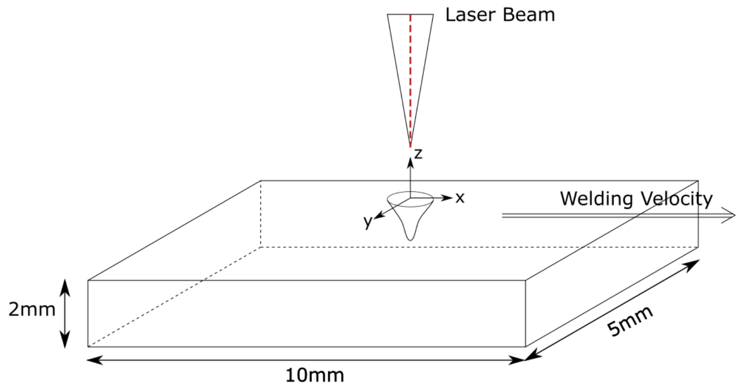

Figure 1. Geometry of the computational domain [13]

Table 1. Three mesh densities

	x	y	z	Total cells	Total faces
Coarse	100	50	20	92,169	284,170
Medium	200	100	40	768,339	2,336,340
Fine	400	200	80	6,272,679	18,944,680

The number of nodal points in x, y and z directions can be found in Table 1. To select the most appropriate time step size, three different levels of the CFL number were studied. It turns out that CFL=5 is too large and CFL=0.1 is not necessary to obtain a reasonable computational cost. These results are summarized in Table 2.

Table 2. Different time steps with different CFL numbers at different mesh densities

CFL Number	Time step (coarse)	Time step (medium)	Time step (fine)
0.1	1e-5	5e-6	2.5e-6
1	1e-4	5e-5	2.5e-5
5	5e-4	2.5e-4	1.25e-4

Three different physical times were investigated, 40 ms, 80 ms, and 120 ms, to select the best physical time scales of the welding process which were simulated. It is important to note that the physical time here means the time scales of the simulated welding process; therefore, these values are not related to the computational time. The effect of mesh sensitivity on the numerical results has been investigated in conjunction with the temperature field, and one can see in Figure 2 that the temperature contours using different mesh densities are almost identical. Figure 3 shows the temperature profiles along the center x line using three different mesh densities, which shows again that the predicted temperature profiles are very similar to each other.

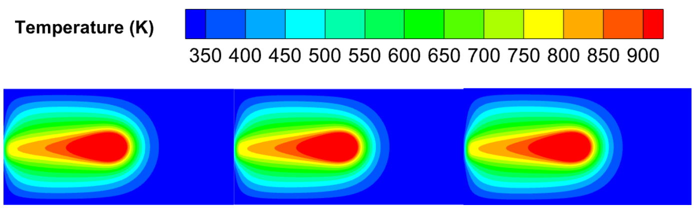

Figure 2. Temperature contour on x-y plane using three different meshes

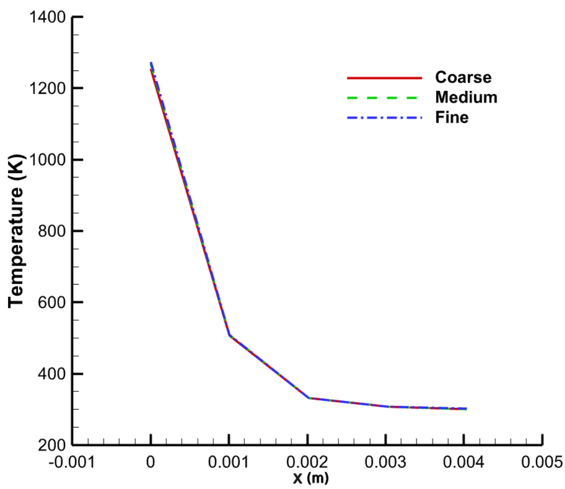

Figure 3. Temperature along the line x using three different meshes

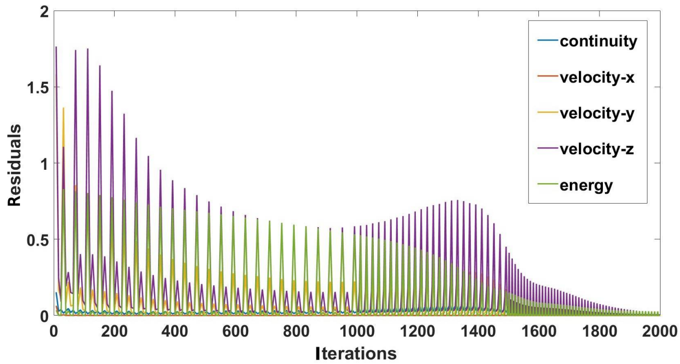

Figure 4. Residuals with CFL = 1 at 40 ms on the coarse mesh

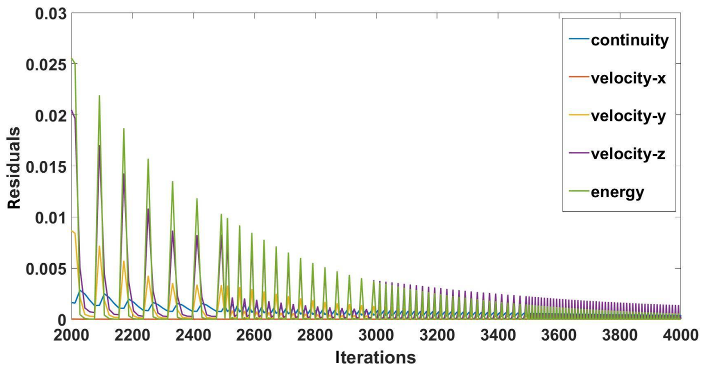

Figure 5. Residuals with CFL = 1 at 80 ms on the coarse mesh

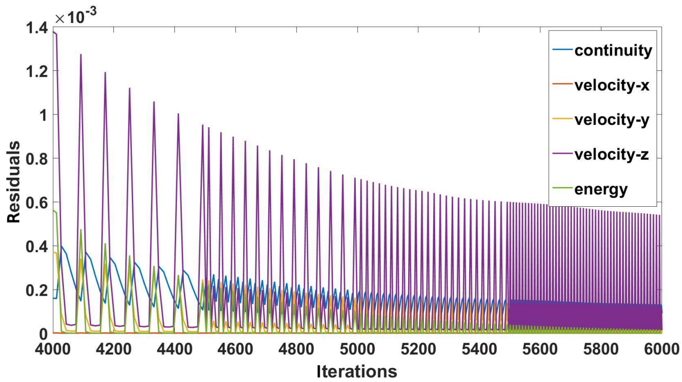

Figure 6. Residuals with CFL = 1 at 120 ms on the coarse mesh

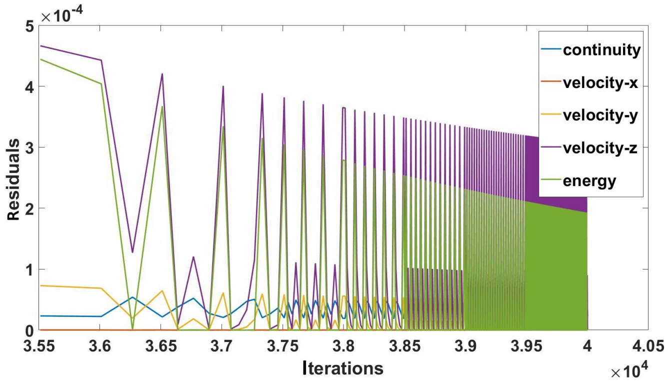

Figure 7. Residuals with CFL = 0.1 at 80 ms on the coarse mesh

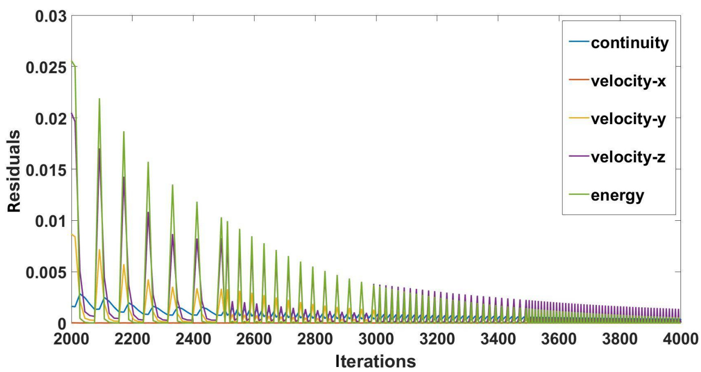

Figure 8. Residuals with CFL = 1.0 at 80 ms on the coarse mesh

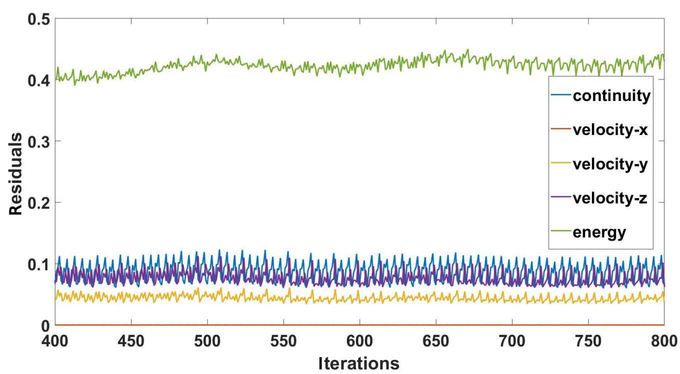

Figure 9. Residuals with CFL = 5.0 at 80 ms on the coarse mesh

To reduce computational time, based on the mesh sensitivity study on the numerical results (see Table 1 and Figures 2 and 3), the coarse mesh has been selected for the final simulations. Figures 4, 5, 6 show the residuals at three physical times. As can be seen in Figure 4, the residuals decline within 40 ms physical time, although they increase at the beginning of the simulations. Similarly to Figure 4, the residuals within 80 ms decline to 10 order of magnitude, which is much bigger than the residual obtained within 40 ms. However, after 80 ms, the residuals reach a statistical steady-state solution. Therefore, this simulation runs 80 ms physical time.

Figures 7, 8, 9 show the residuals with three different CFL numbers. One can see that the residual with CFL=1 is steady state, which is equal to 10^{-3} while it is 10^{-1} with CFL=5. Therefore, for the final simulations, CFL=1 has been selected. Thus, the time step of this model is 10^{-4} (see Table 2). To investigate different parameters, various benchmark test cases have been simulated, which are summarized in Table 3 and discussed in the next section.

Table 3. Different validation test cases

	Welding speed (m/min)	Laser power (W)	Shear stress (Pa)
case 1	1	700	6.40E-04
case 2	5	700	6.40E-04
case 3	10	700	6.40E-04
case 4	1	1000	6.40E-04
case 5	5	1000	6.40E-04
case 6	10	1000	6.40E-04
case 7	1	2000	6.40E-04
case 8	5	2000	6.40E-04
case 9	10	2000	6.40E-04
case 10	5	2000	6.40E-03
case 11	5	2000	6.40E-02
case 12	5	2000	6.40E-01
case 13 (no convective term)	5	2000	6.40E-04
case 14 (no buoyancy force)	5	2000	6.40E-04

4. Results and Discussion

In this section, simulation results for 12 cases are analyzed at different welding speeds and laser powers to investigate the impact of the welding speed and the laser power effects. In the first part, the temperature is analyzed at different laser powers and welding speeds. Figure 10 shows temperature contours on the top wall on x-y plane. From left to right, they are at welding speeds from 1 m/min to 10 m/min and from top to bottom, they are at different laser powers from 700 W to 2000 W. As can be seen from the figure, with the increase of the welding speed, the maximum temperature decreases. This is due to the fact that with the increase of the welding speed, the interaction time between the laser beam and workpiece decreases so that the workpiece absorbs less energy. In addition, with the increase of the welding speed, the band of the temperature contour becomes longer and with an obvious "tail". This was more obvious at higher laser power.

Regarding the impact of different laser powers, it can be seen from figures that with the increase of the laser power, the maximum temperature on the center of top wall increases. This is reasonable because large laser power means more energy absorption. Moreover, Figure 11 shows the temperature contour on the x-z plane with different laser powers and welding speeds. The layout of this figure is identical with Figure 10 with different laser powers and welding speeds. However, the direction of this figure is in the width direction. As can be seen from the figure that with the increase of the laser power, the maximum temperature in the width direction increases, especially at the lowest welding speed. In term of the impact of the welding speed, the larger welding speed makes the temperature on the center much lower. The band of temperature contour with 5 m/min welding speed was longest among three contours. This is also because of the longer time of interaction between the laser beam and the workpiece.

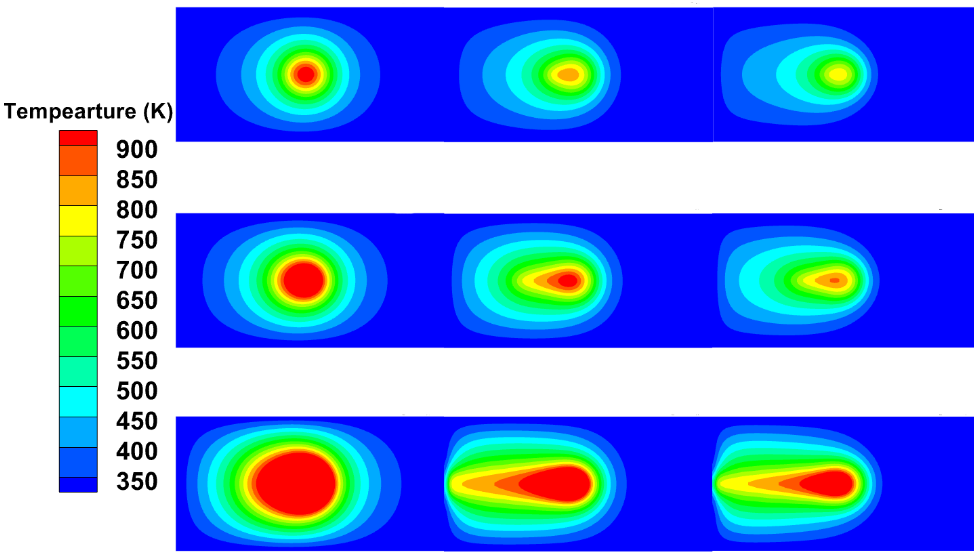

Figure 10. Temperature distribution with different parameters on x-y plane

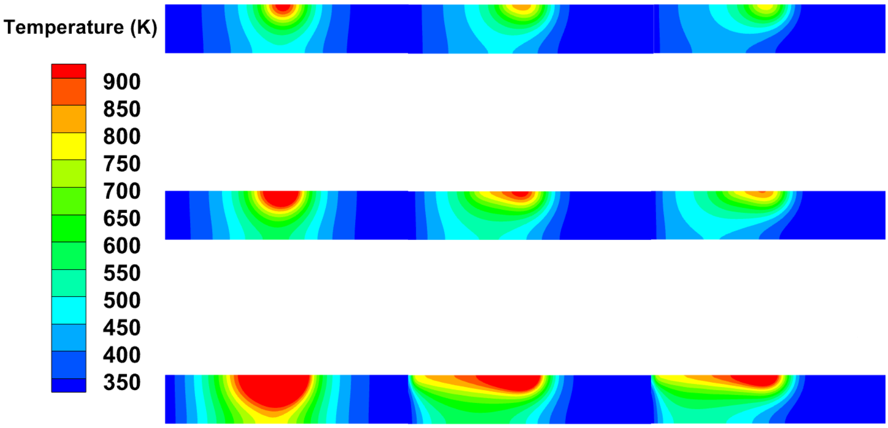

Figure 11. Temperature distribution with different parameters on x-z plane

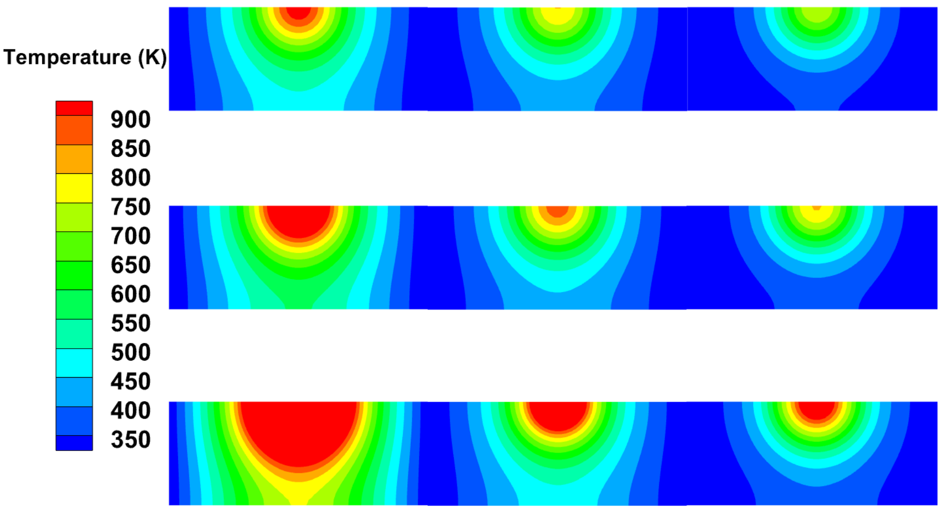

Figure 12. Temperature distribution with different parameters on y-z plane

Figure 12 demonstrates the temperature contour with different laser powers and welding speeds with the same layout as the previous figures in the y-z plane. It can also be seen from figures that with the increase of the laser power, the range of the maximum temperature increases. Another shared feature is that as the welding speed increases, the range of the maximum temperature decreases can also be seen. However, the long "tail" in figures with the increase in welding speed cannot be seen this time, which means the increase of the welding speed does not affect the symmetric feature in the depth direction. The symmetric temperature contour is because of the

Gaussian distribution heat source implemented in the energy equation. If a very low welding speed was implemented, the symmetrical feature was kept. More detailed effects of different welding speeds and laser powers can be seen in Figure 13.

In addition, Figures 10, 11, 12 show the Gaussian thermal distribution, which was implemented as a source term, with high temperature in the center, decreasing to the outside.

Figure 13(a) displays the temperature along the center x line with different welding speeds and laser powers. The same features were also seen in this figure. With respect to the welding speed, in Cases 1, 2 and 3, the maximum temperature decreases with the increase of the welding speed. In addition, there are always two parts of the curves: the first part is from bottom to the maximum temperature, and the second part is from the maximal part to the top. The same features can be seen with Cases 4, 5 and 6, although a certain amount of distortion can be observed in the first part of the curves. Similar features can be seen in Cases 7, 8 and 9. Larger distortion can be seen from the first part of the curve in Cases 8 and 9, which means that with higher laser power, the increase of the welding speed leads to larger distortion of the temperatures near the rear part of the workpiece.

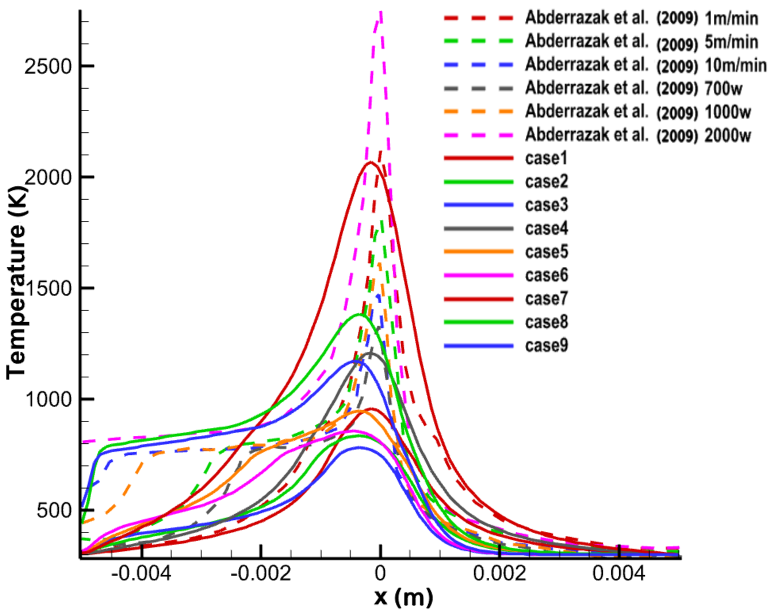

(a)

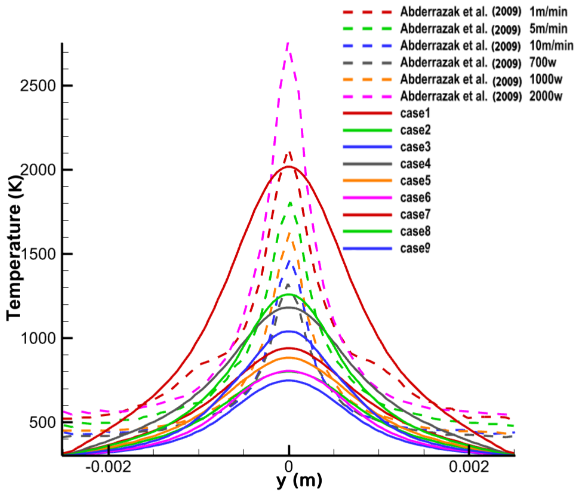

(b)

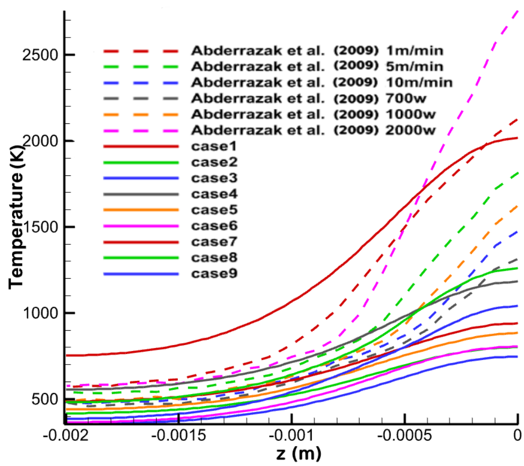

(c)

Figure 13. Temperature distribution with different laser power and welding speeds in comparison with the results of Abderrazak et al. [13] along x, y and z lines

With respect to the laser power, the maximum and overall temperature increases with the increase of the laser power in Cases 1, 4 and 7. This can also be seen from

Cases 2, 5 and 8 as well as 3, 6 and 9. In comparison with the results of Abderrazak et al. [13], it is also like a ring-bell shape curve. In addition, certain distortions are present at the beginning part of the curve, as can be seen in a few cases. Moreover, the results of the peak temperature of 2000 W of Abderrazak et al. [13] is larger than for the implemented model. The results of the shape of Abderrazak et al. [13] are a bit narrower than those of the implemented model. The combination of case settings pertaining to welding speed and laser power in the work of Abderrazak et al. [13] are not shown; therefore, the discrepancy between the reference paper and results of the implemented model is in an acceptable range. In other words, the overall shape generated by the implemented model and that of Abderrazak et al. [13] is similar.

Figure 13(b) presents the center y line with different welding speeds and laser powers. The same features with previous contours were also seen in this figure. However, distortions cannot be seen in this figure, unlike in Figure 13(a). With respect to the welding speed, Cases 1, 2 and 3 also show the trend that is similar to Figure 13(a). The same feature can be seen in Cases 4, 5 and 6 as well as 7, 8 and 9. There are also two parts of the curves, one of which is from negative y value part to the zero value and the other of which is from zero to positive y value part. In terms of the laser power, the same feature that the increase of the laser power increases the temperature can be seen in Cases 1, 4 and 7 as well as 2, 5 and 8 also 3, 6 and 9.

However, one thing worth noting is that the temperature along the center y line is almost identical with that of Cases 2 and 5. In comparison with the results obtained by Abderrazak et al. [13], it is also symmetrical. However, there are distortions in two sides of the results of Abderrazak et al. [13] with 1 m/min welding speed. Moreover, the results of the shape of Abderrazak et al. [13] are narrower than the implemented model as well. In addition, the temperature on the edge of the curve in the work of Abderrazak et al. [13] is a bit bigger than in the implemented model. However, as the combination of case settings pertaining to the welding speed and the laser power in the work of Abderrazak et al. [13] is not shown, some discrepancy between the reference paper and results with the implemented model is expected.

Figure 13(c) demonstrates the temperature along the center z line with different welding speeds and laser powers. In contrast to Figure 13(b), there is only one part of the curve, the temperature increases along the center z line, whose slope slowly increases and finally decreases to a plateau. However, with respect to the welding speed, Cases 1, 2 and 3 as well as 4, 5 and 6 also 7, 8 and 9 show the similar trend with previous contours and previous curves along x and y line. This is also true with respect to laser power. It is also interesting to note that Cases 2 and 5 have almost identical temperature, which is the same with Figure 13(b) for temperature along the center y line. In comparison with the results of Abderrazak et al. [13], the overall shape is an upward trend. However, the part behind -0.001 of the results of the slope in Abderrazak et al. [13] is higher than that of the implemented model, especially the one with 2000 W. Nevertheless, as the combination of case settings pertaining to the welding speed and the laser power in the work of Abderrazak et al. [13] is not given, a discrepancy between the reference paper and results with the implemented model is reasonable.

Figure 14 demonstrates the velocity contour on the top x-y plane with different laser powers from top to bottom and welding speeds from left to right. It can be seen from the figure that with the increase of the laser power, the range of maximum velocity becomes larger. However, it does not always decrease with the increase of the welding speed; the velocity contour with 5 m/min welding speed has the largest range of maximum velocity. Moreover, with 1000 W and 2000 W laser power, the velocity contour with 5 m/min and 10 m/min welding speed is almost identical. It is also interesting to note that with the laser power of 2000 W, the gradient of the velocity contour is much smaller. In addition, with the increase of the welding speed, the range of maximum velocity shrinks.

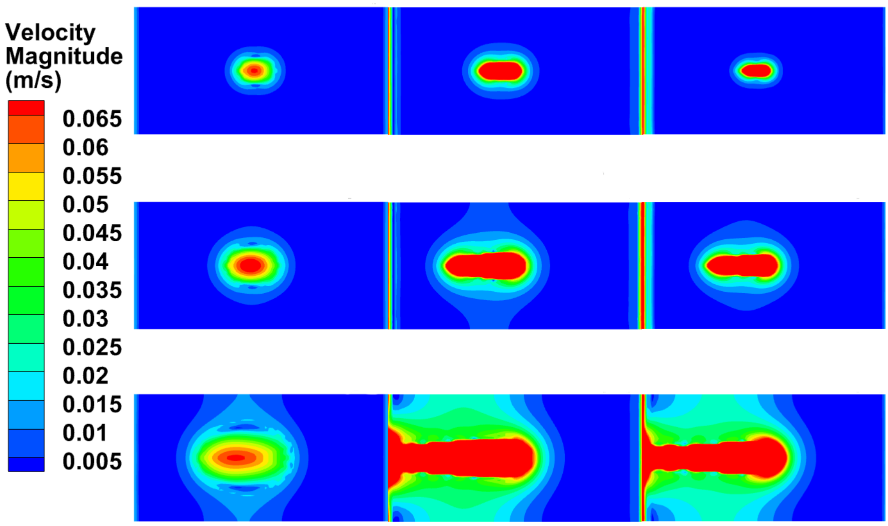

Figure 14. Velocity distribution with different parameters on x-y plane

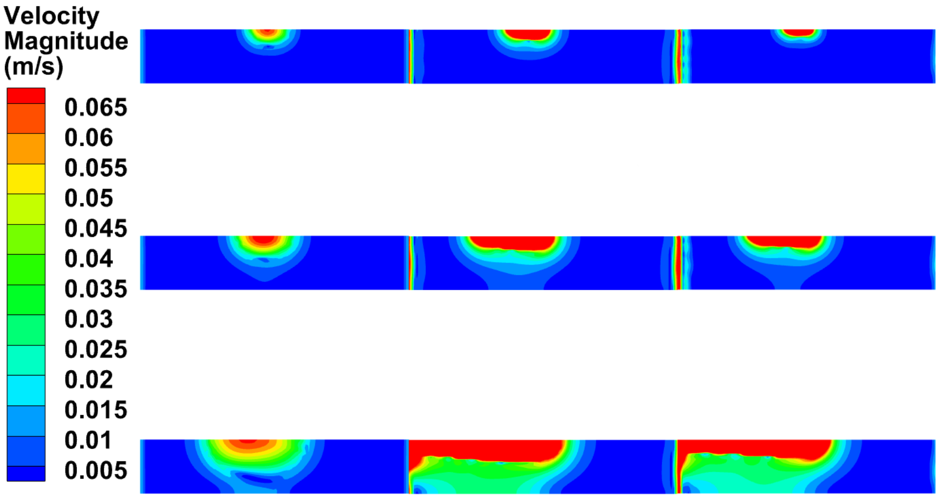

Figure 15. Velocity distribution with different parameters on x-z plane

Figure 15 shows the velocity contour on width direction on the x-z plane. It can also be seen from the figure that with the increase of the laser power from top to bottom, the range of velocity value greater than zero becomes larger. In terms of the welding speed, the velocity increase with the increase of the welding speed until 5 m/min. However, the velocity with 5 m/min and 10 m/min is almost the same. In addition, the increase of the welding speed also makes the tail of velocity contour much longer. This is similar to the temperature contour in the previous figures.

Figure 16 displays the velocity contour in the depth direction with different welding speeds and laser powers. The increase in the velocity contour with the increase of the laser power from bottom to top can also be seen from these figures. However, a special case is found with the welding speed of 1 m/min, where the velocity of maximum range decrease from with 1000 W to 2000 W. In addition, the increase of the welding speed does not make the long tail in the depth direction. In contrast to the temperature contour, there is no increasing trend with the increase of the welding speed. Moreover, the contours for 1 m/min and 5 m/min welding speed are almost identical, especially at 1000 W and 2000 W laser power.

In addition, the velocity contour also shows the Gaussian distribution feature, althoughthe Gaussian feature of velocity contour is not as strongly developed as with the temperature contour. The most symmetrical velocity contour is on the y-z plane in Figure 16. Thus, the velocity develops more strongly than the temperature contour. In comparison with the velocity results of Abederrazak et al. [13], the maximum velocity region of the center is bigger due to different boundary condition settings.

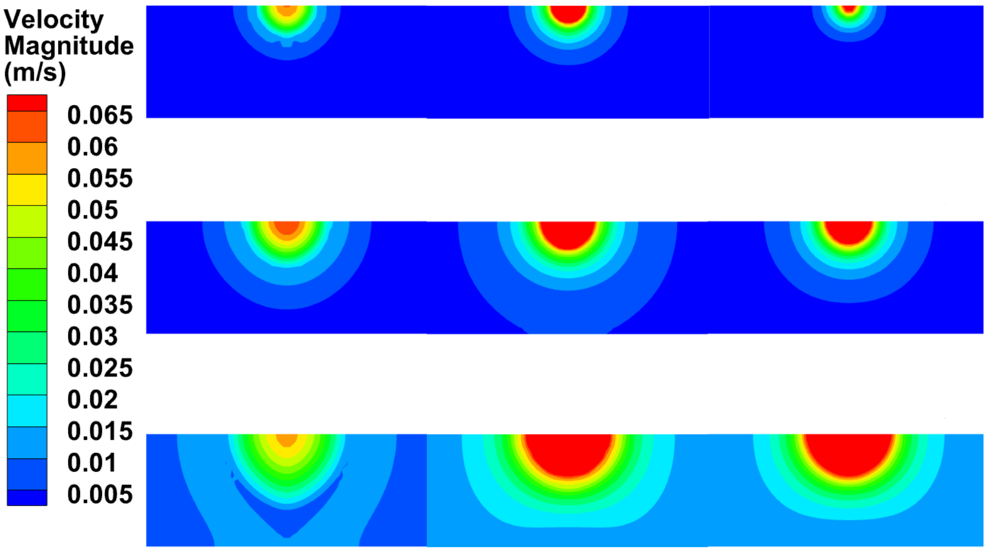

Figure 16. Velocity distribution with different parameters on y-z plane

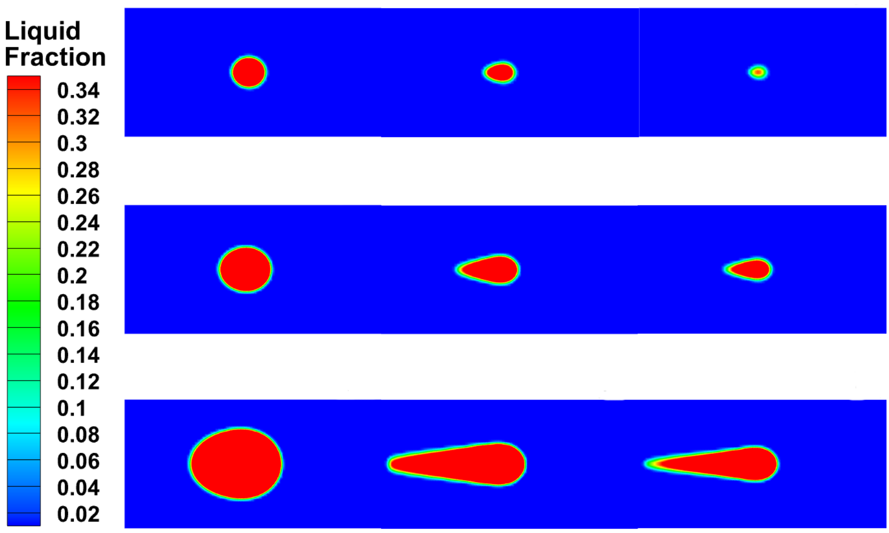

Figure 17. Liquid fraction with different parameters on x-y plane

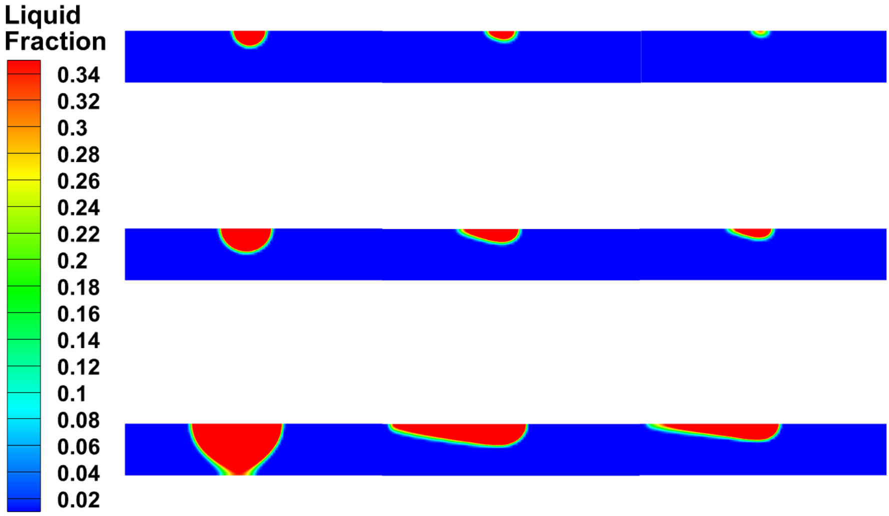

Figure 18. Liquid fraction with different parameters on x-z plane

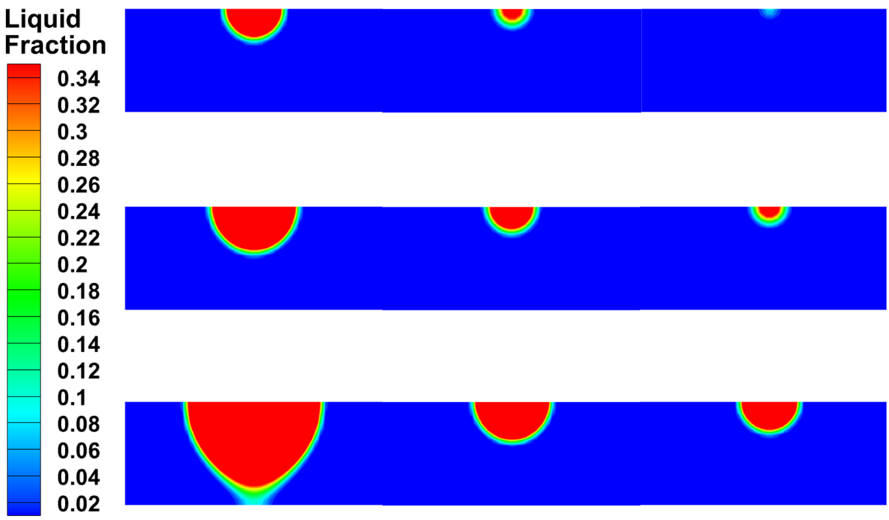

Figure 19. Liquid fraction with different parameters on y-z plane

Figure 17 demonstrates the liquid fraction on the top wall on the x-y plane with different laser powers and welding speeds. The same feature of temperature contours can be seen in this figure. In term of the laser power, the melting fraction becomes larger as the laser power increases. Regarding the welding speed, it also be seen that a longer tail is formed with the increase of the welding speed. However, with the increase of the welding speed with the laser power of 700 W, the tail did not form, and only a small liquid fraction is present.

Figures 18 and 19 show the liquid fraction on the width and depth direction respectively. As can be seen from the figures, with the laser power increase, the liquid fraction increases both in width and depth. However, in the width direction, the long tail forms with the increase of the welding speed. In contrary, the tail does not form in the depth direction. It is also worth noting that with 700 W laser power and 10 m/min welding speed, the liquid fraction is very small both in width and depth direction.

Figure 20 shows a different pool shape with different velocity from left to right with different laser powers : 700 W, 1000 W, and 2000 W. From this figure, the long tail shape of the pool produced by the welding speed can be seen; with higher laser power, the length of tail is longer than with lower laser power. In addition, with the laser power increase, the pool shape becomes narrower at the same welding speed. It is also worth noticing that with 2000 W laser power and 1 m/min welding speed, the depth of penetration is the largest, penetrating almost the entire depth of the workpiece. Moreover, with the increase of the laser power, the center region of largest liquid increase. In terms of depth of the pool, the increase in the welding speed makes the pool shape shallower, while the laser power with small welding speed makes the pool shape deeper. Finally, the welding speed distortion impact with lower laser power is much less obvious, while the pool shape with 1000 W and 2000 W laser power becomes upward, with a longer tail, and more distorted with higher welding speed.

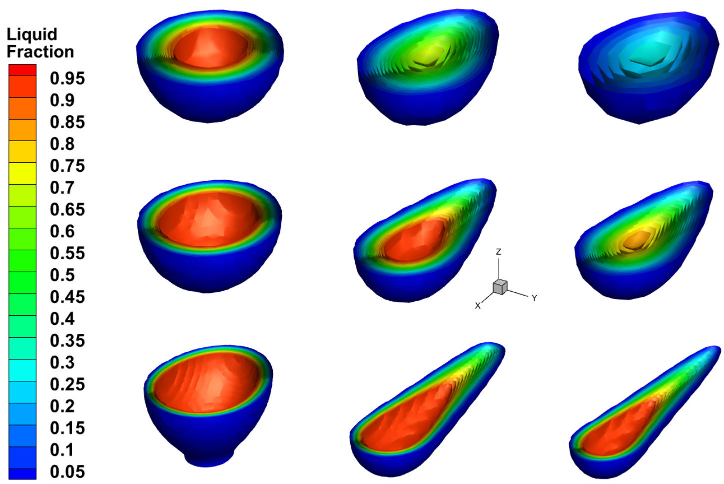

Figure 20. Pool shape with different parameters

Figure 21(a) shows the penetration depth with respect to the laser power at three different welding speeds. It can be seen from the figure that as the laser power increases, the penetration depth also increases. However, with 1 m/min welding speed, the penetration depth increases more than with 5 m/min and 10 m/min welding speeds from 1000 W to 2000 W laser power. From the range of 700 W to 1000 W, the penetration depth with three different welding speeds does not differ much. In addition, the penetration depth with 5m/min is quite similar to the results of Abderrazak et al. [13], especially with 1000 W laser power. There is little difference at 700 W and 2000 W between the two models.

Figure 21(b) demonstrates the penetration depth with respect to the welding speed at three different laser powers. As can be seen from the figure, as the welding speed increases, the penetration depth decreases, which was seen as well in the previous analysis. In addition, it is worth noting that at 2000 W laser power with the increase of the welding speed from 1 m/min to 5 m/min, the penetration depth decreases more than with lower laser power. With the increase of welding speed from 5 m/min to 10 m/min, the three penetration depths decrease to a similar degree with respect to the welding speed. This is very similar to the results of Abderrazak et al. [13] at 1000 W, especially at 1 m/min welding speed.

Figures 21(c) and 21(d) show the bead width respect to three different laser powers and three different welding speeds, respectively. It can be seen from these two figures that with the increase of the laser power the bead width of the pool increases, while it decreases with increased welding speed. Moreover, at 2000 W laser power, the bead width decreases more from the welding speed 1 m/min to 5 m/min than with lower laser power. Finally, with 1 m/min welding speed, the bead width increases more from laser power 700 W to 1000 W than with higher welding speed. This feature was also seen in the previous analysis. The reason for this may be that with lower welding speed, the interaction time between the laser beam and the workpiece is longer, so the increase in the laser powermore strongly affects the bead width. In terms of the high laser power, the increase of the welding speed leads to more energy loss with higher laser power. Regarding the comparison with the results of Abderrazak et al. [13], the bead width at 700 W is similar to the numerical values obtained by Abderrazak et al. [13]. Moreover, the bead width for 10 m/min welding speed is also similar to their results, except at 1000 W laser power.

Figures 22, 23, 24 are contours of temperature, velocity and liquid fraction at different planes with and without buoyancy force. As can be seen from the figures, the results with and without buoyancy force are almost identical. Thus at least in the implemented model settings, the buoyancy force does not have much impact on the results.

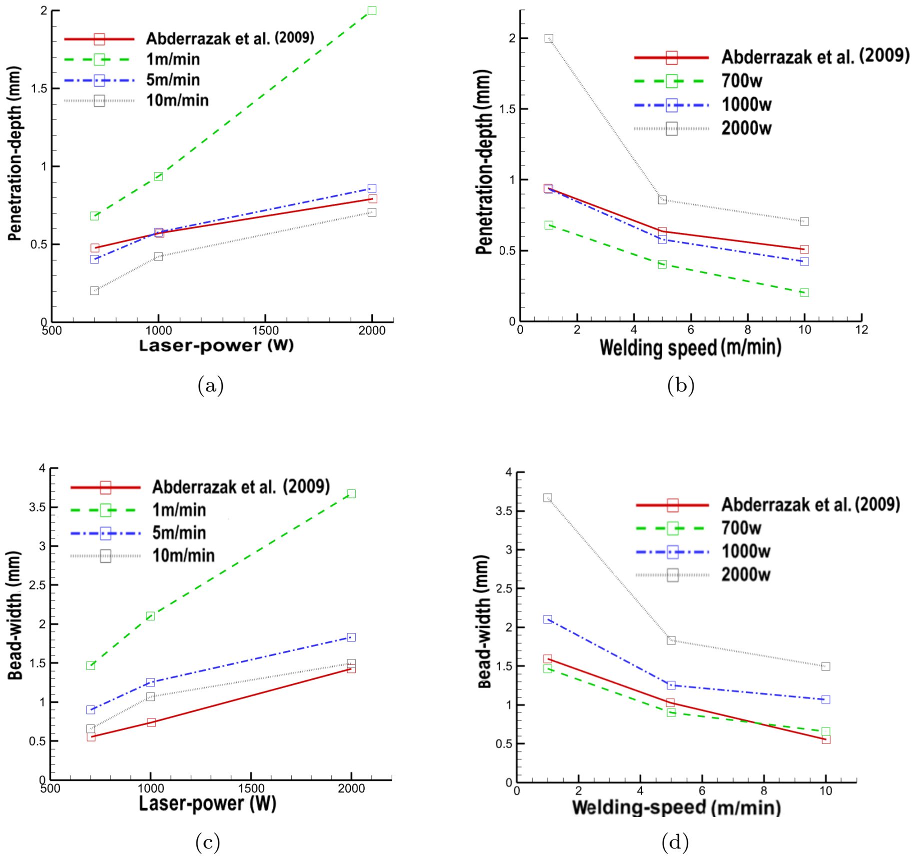

Figure 21. Penetration depth and bead width with different parameters compared to the results of Abderrazak et al. [13]

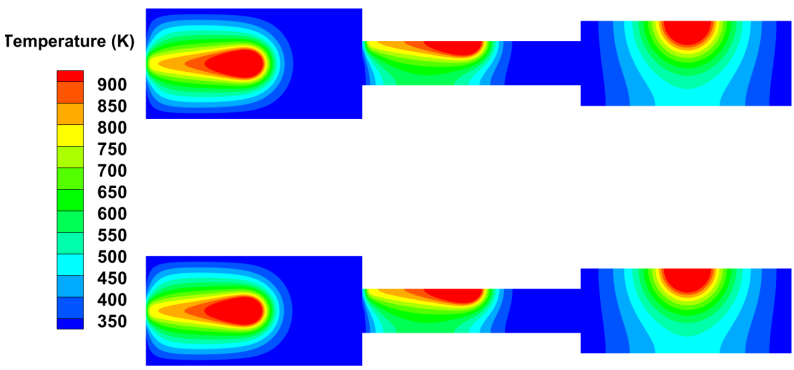

Figure 22. Temperature with and without taking the buoyancy force into account

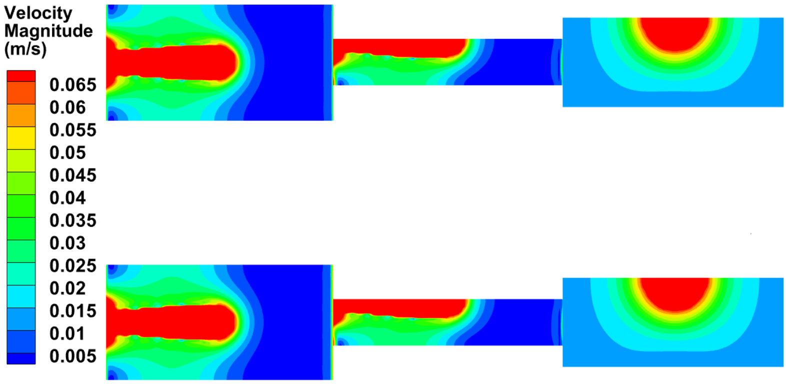

Figure 23. Velocity with and without taking the buoyancy force into account

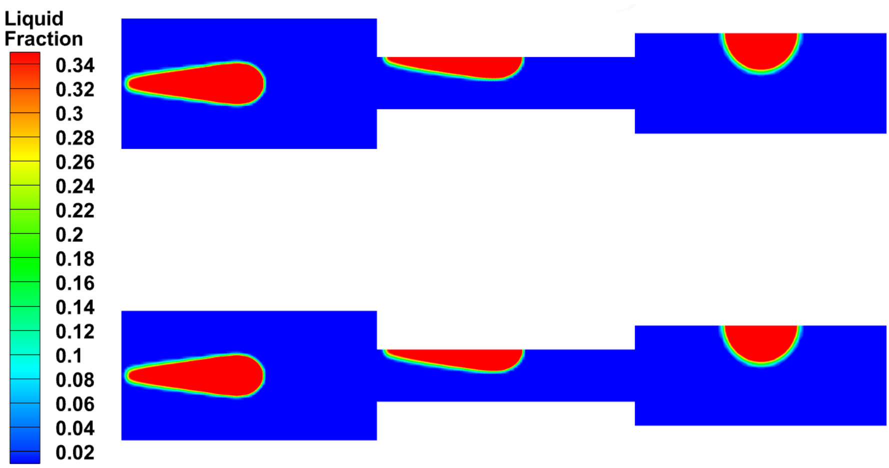

Figure 24. Liquid fraction distributions with and without taking the buoyancy force into account

In this work, we analyze the influence of buoyancy force on temperature, velocity and liquid fraction in comparison with the work of Abederrazak et al. [13] which can be considered as a novelty of this paper.

Figures 25, 26, and 27 display the temperature, velocity and liquid fraction contour with and without the convective term in the energy equation in different planes, respectively. As can be seen from Figure 25, the maximum temperature range increases without the convective term in the energy equation in the entire three planes. This is true because the convective term enhances the convection so that the pool shape becomes smaller and the maximum temperature range is much lower.

Figure 26 presents the velocity contour with and without the convective term in energy equation. As can be seen from the figure, without the convective term, the maximum velocity range becomes larger, especially in the depth and length directions. In the length direction, without the convective term, the maximum velocity range becomes wider. In the depth direction, the maximum velocity range becomes wider, while a lower number of velocity bands was seen without the convective term.

Figure 27 shows the liquid fraction with and without the convective term in the energy equation. It can be seen that without the convective term, the liquid fraction in all three planes is slightly larger than that with the convective term. This might be because without the convective term, there is no heat exchange between the hot liquid and cold solid so that the pool gets more heat, which makes a bigger pool shape.

As stated before, the analysis of convective term is also one of the novelty of this paper compared with Abederrazak et al. [13] Moreover, the influence of the convective term has an impact on the velocity due to the fact that convection produces changes in velocity while it has almost no impact on temperature and liquid fraction with the current boundary settings.

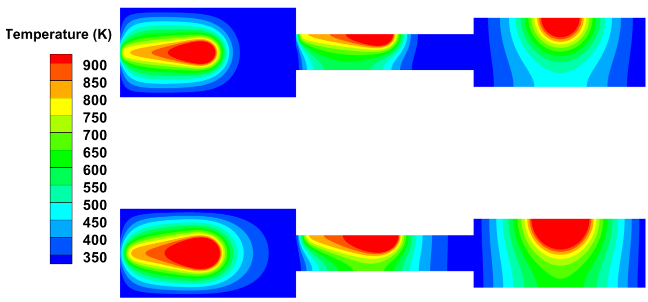

Figure 25. Temperature with and without taking the convective term into account

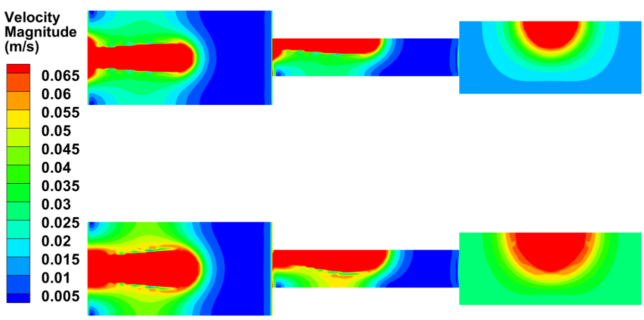

Figure 26. Velocity with and without taking the convective term into account

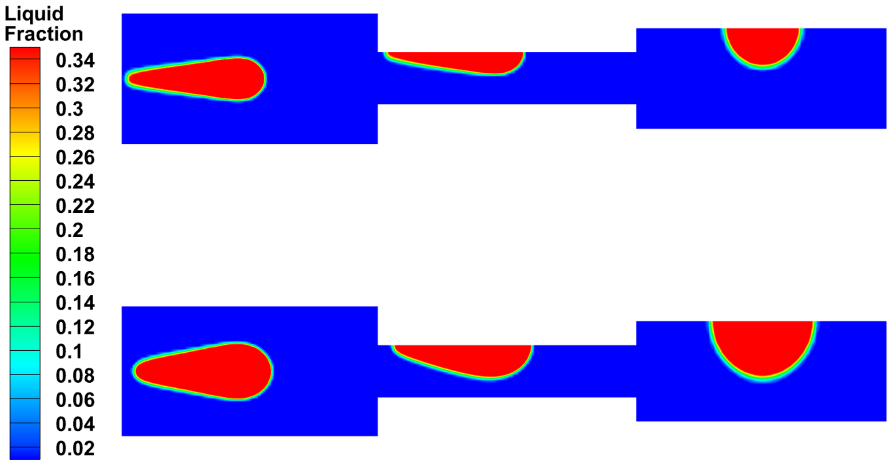

Figure 27. Liquid fraction distributions with and without taking the convective term into account

The effect of negative Marangoni force with three different shear stresses (6.4e-3 Pa, 6.4e-2 Pa and 6.4e-1 Pa) was investigated for Cases 10, 11 and 12. Figure 28 shows the velocity magnitude along the center x line with different shear stresses. As can be seen from the figure, the velocity magnitude is almost identical for the three different shear stresses. Figure 29 displays the velocity magnitude along the center y line. As can be seen from the figure, the results of Cases 10 and 11 are almost identical. While for Case 12 with the largest shear stress, the velocity magnitude in the center is lower than in the other two cases, while the velocity is larger at the edge of the workpiece. Figure 30 gives the velocity magnitude along the center z line. The figure shows that with smaller shear stress for Cases 10 and 11, the results are almost identical. For Case 12, with the largest shear stress, the velocity is a bit smaller than the other two cases near the top wall of the workpiece, while the velocity magnitude in the center is lower and the velocity is higher at the edge of the workpiece. Figure 30 is the velocity magnitude along the center z line. The figure shows that with smaller shear stress for Case 10 and 11, the results are almost identical, while near the top wall of the workpiece, Case 12 has lower velocity than the other two cases.

In addition, the Marangoni effect is also an important effect in laser welding application. Abederrazak et al. [13] did not analyze the specific influence of the Marangoni effect. Thus the analysis of the Marangoni effect is also one of the novelties of this paper. Through Figures 29 and 30, it can be seen that the Marangoni effect mainly affects flow in the y and z directions, which is in accordance with the definition of the Marangoni effect, because the Marangoni effect is due to the fact that surface tension gradient is different in y and z, while in the x direction, the surface tension gradient is almost identical.

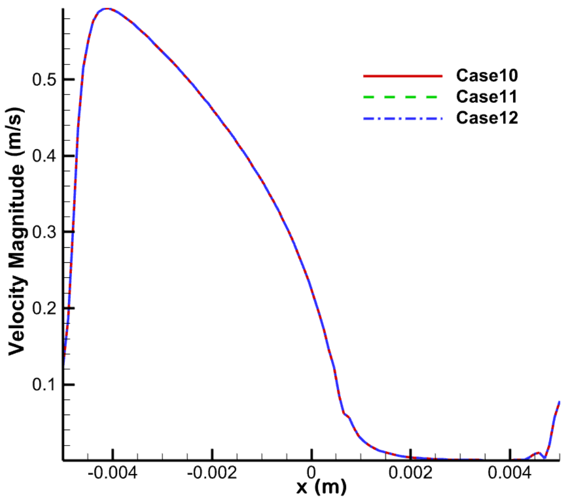

Figure 28. Velocity distribution with different shear stresses along x line

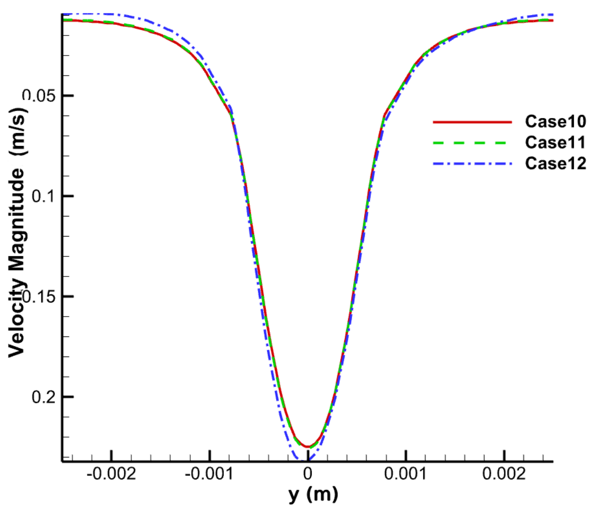

Figure 29. Velocity distribution with different shear stresses along y line

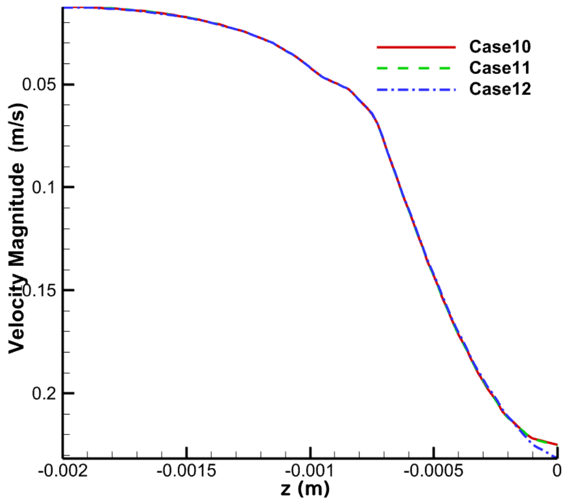

Figure 30. Velocity distribution with different shear stresses along z line

Figures 31, 32, and 33 show the velocity vector with Cases 10, 11 and 12 with different shear stresses. As can be seen in the figures, there are two vertices in Case 10, which is also mentioned in Abderrazak et al. [13]. However, with the increase of the shear stress, the two main vertices are not that obvious, as can be seen in Figure 32 and Figure 33.

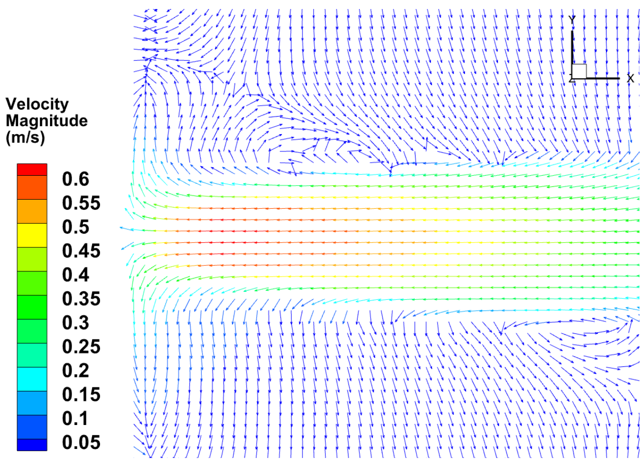

Figure 31. Velocity vector for Case 10

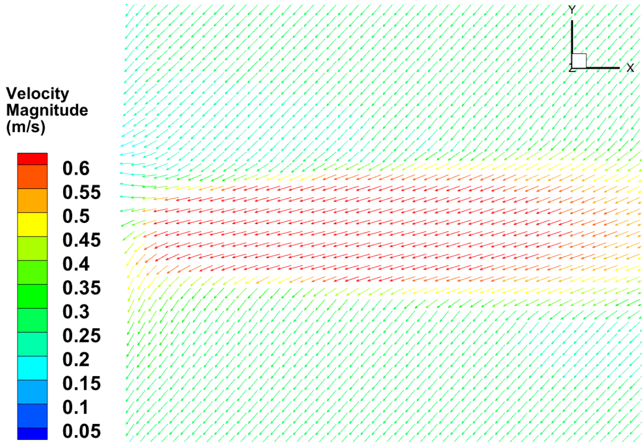

Figure 32. Velocity vector for Case 11

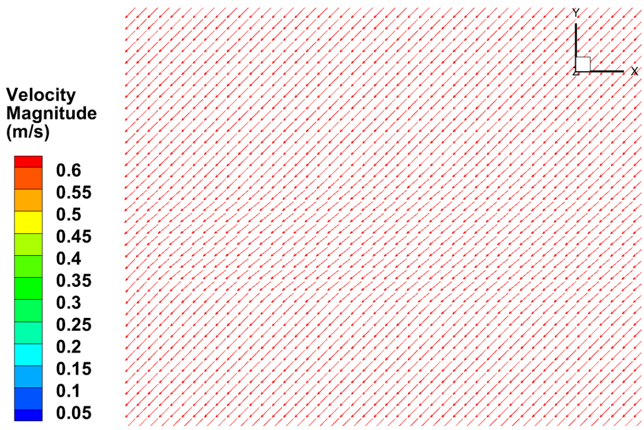

Figure 33. Velocity vector for Case 12

5. Conclusions and Recommendations

According to previous results and discussion, the following conclusions can be drawn:

- With the increase of the welding speed, the temperature and liquid fraction decreases and the contour forms a longer "tail" in width and length directions. However, velocity does not always decrease;
- Increasing the laser power leads to an increase in temperature, liquid fraction and velocity in all planes, which can also be seen from the temperature curves;
- The pool shape becomes more distorted and moves upward with larger welding speed and laser power;

- With the increase of the laser power, the penetration depth and bead width increase. With the increase of the welding speed, the penetration depth and welding speed decrease;
- Different shear stresses do not have much impact on the results of velocity magnitude along the center x line. However, along the center y line, the largest shear stress has the lowest velocity magnitude in the middle and the largest value on the edge of the workpiece. Moreover, along the center z line, the largest shear stress leads to the lowest velocity magnitude on the top of the wall. In addition, two vertices can be seen in Case 10 of this model, while with the increase of shear stress, the vertices become less obvious;
- Buoyancy force in this model does not make much difference to the results for velocity, temperature and liquid fraction;
- Without the presence of the convective term in the energy equation, the liquid fraction, temperature and velocity are higher than with the convective term in the energy equation.

Although several results were achieved based on this numerical model, there are still many extensions that can be done in the future. They are summarized as follows:

- The pool shape on the top wall was assumed to be flat; future work can remove this assumption and add a free surface tracking algorithm such as VOF or the level-set method;
- The laser beam in this model is a simple model that did not consider absorption or reflection. Future work can add a more realistic model of laser beam;
- The recoil pressure was not considered in this model; future work can add this feature;
- Other phenomena such as evaporation or plasma plume can also be added to this model in future work.

Acknowledgement. This project was financially supported by the Centre for Computational Engineering Sciences at Cranfield University under project code EEB6001R. For the purpose of open access, the authors have applied a Creative Commons Attribution (CC BY) licence to any author accepted manuscript version arising. Furthermore, we would like to acknowledge the IT support for using the High Performance Computing (HPC) facilities at Cranfield University, UK.

References

1. Steen, W. M. "Laser material processing-an overview." *Journal of Optics A: Pure and Applied Optics,* **5**(4), (2003), S3. doi: 10.1088/1464-4258/5/4/351.
2. Shin, Y. C., Benxin, W., Shuting, L., Gary, J. C., and Yao, Y. L. "Overview of Laser Applications in Manufacturing and Materials Processing in Recent Years." *Journal of Manufacturing Science and Engineering,* **142**(11), (2020). doi: 10.1115/1.4048397.
3. Eriksson, I., Gren, P., Powell, J., and Kaplan, A. "New high-speed photography technique for observation of fluid flow in laser welding." *Optical Engineering,* **49**(10) (2010), p. 100503. doi: 10.1117/1.3502567.

4. Norman, P., Engström, H., and Kaplan, A. "Theoretical analysis of photodiode monitoring of laser welding defects by imaging combined with modelling." *Journal of Physics D: Applied Physics,* **41**(19), (2008), p. 195502. doi: 10.1088/0022-3727/41/19/195502.
5. Zhang, Yanxi, Gao, Xiangdong, You, Deyong, and Zhang, Nanfeng. "Data-driven detection of laser welding defects based on real-time spectrometer signals." *IEEE Sensors Journal,* **19**(20) (2019), pp. 9364–9373. doi: 10.1109/JSEN.2019.2927268.
6. Swift-Hook, DT and Gick, AEF. "Penetration welding with lasers." *Welding journal,* **52**(11), (1973), 492s–499s.
7. Lankalapalli, Kishore N., Tu, Jay F., and Gartner, M. "A model for estimating penetration depth of laser welding processes." *Journal of Physics D: Applied Physics,* **29**(7), (1996), p. 1831. doi: 10.1088/0022-3727/29/7/018.
8. Dowden, J., Kapadia, P., and Postacioglu, N. "An analysis of the laser-plasma interaction in laser keyhole welding." *Journal of Physics D: Applied Physics,* **22**(6), (1989), p. 741. doi: 10.1088/0022-3727/22/6/004.
9. Carmignani, C., Mares, R., and Toselli, G. "Transient finite element analysis of deep penetration laser welding process in a singlepass butt-welded thick steel plate." *Computer methods in applied mechanics and engineering,* **179**(3-4), (1999), pp. 197–214. doi: 10.1016/S0045-7825(99)00043-2.
10. Ye, Xiao-Hu and Chen, Xi. "Three-dimensional modelling of heat transfer and fluid flow in laser full-penetration welding." *Journal of Physics D: Applied Physics,* **35**(10), (2002), p. 1049. doi: 10.1088/0022-3727/35/10/313.
11. Ki, Hyungson, Mohanty, PS, and Mazumder, Jyoti. "Modelling of high-density laser-material interaction using fast level set method." *Journal of Physics D: Applied Physics,* **34**(3), (2001), p. 364. doi: 10.1088/0022-3727/34/3/320.
12. Geiger, M., Leitz, K. H., and Koch, H. and Otto, A. "A 3D transient model of keyhole and melt pool dynamics in laser beam welding applied to the joining of zinc coated sheets." *Production Engineering,* **3**(2), (2009). doi: 10.1007/s11740-008-0148-7.
13. Abderrazak, K., Bannour, S., Mhiri, H., Lepalec, G., and Autric, M. "Numerical and experimental study of molten pool formation during continuous laser welding of AZ91 magnesium alloy." *Computational Materials Science,* **44**(3), (2009), pp. 858–866. doi: 10.1016/j.commatsci.2008.06.002.